REFERENCES AND NOTES

1. B. J. Mason, *The Physics of Clouds* (Clarendon, Oxford, 1971), p. 174.
2. K. Sassen, D. O'C. Starr, T. Uttal, *J. Atmos. Sci.* **46**, 371 (1989).
3. A. J. Heymsfield and R. M. Sabin, *ibid.*, p. 2252.
4. K. Sassen and G. C. Dodd, *ibid.*, p. 3005.
5. It is more accurate to refer to these droplets as haze particles, because at such low temperatures they probably remain in environmental equilibrium below their critical radii until freezing.
6. K. Sassen, *Bull. Am. Meteorol. Soc.* **72**, 1848 (1991).
7. ———, K. N. Liou, S. Kinne, M. Griffin, *Science* **227**, 411 (1985).
8. We have regularly collected polarization ruby lidar data from cirrus clouds since 1987 in support of the Extended Time Observations component of Project FIRE.
9. Local Project FIRE radiosonde data have provided atmospheric temperature and wind information, based on the use of a time-weighted average of high-resolution (~40 m) data obtained at 0030 and 0905 UTC on 6 December 1991.
10. K. Sassen, C. J. Grund, J. D. Spinhirne, M. M. Hardesty, J. M. Alvarez, *Mon. Weather Rev.* **118**, 2288 (1990).
11. The question of the ambiguity in PDL cloud phase discrimination deserves discussion. Near-zero δ values can be produced by homogeneous spheres, plate crystals large enough (≥250 μm in diameter) to orient horizontally, and aspherical particles smaller than the incident wavelength (air molecules). The rapidly rising turrets (note the absence of wind shear effects) in Fig. 3 must contain relatively small particles, certainly too small to orient uniformly. On the other hand, laboratory experiments with artificially "seeded" supercooled clouds demonstrate that minute frozen droplets rapidly grow the facets needed to produce optical depolarization [K. Sassen and K. N. Liou, *J. Atmos. Sci.* **36**, 852 (1979)]. Lidar observations of aircraft condensation trails and glaciating clouds (*7*) show the same rapid transition in δ as ice crystals form. Although some ice nucleation probably took place in the cell heads, we conclude that liquid droplet backscattering predominated.
12. Cloud-forming nuclei derived from at or near the Earth's surface are deficient at cirrus altitudes because of sedimentation. Lidar studies of cirrus clouds that straddle high tropopauses have revealed unusual cloud properties that probably reflect the effects of stratospheric-derived CCNs [K. Sassen, *Appl. Opt.* **30**, 3421 (1991)].
13. It is also possible that the sulfuric acid droplets could freeze directly into ice crystals during growth from tropospheric water vapor.
14. K. Sassen *et al.*, *Appl. Opt.* **28**, 3024 (1989).
15. K. Sassen and J. D. Horel, *J. Atmos. Sci.* **47**, 2881 (1990).
16. Preliminary supporting remote and in situ data from Project FIRE have shown directly the mixing of stratospheric ozone and volcanic aerosols into the cirrus cloud altitude during this period.
17. For example, Mie scattering theory simulations reveal that a water droplet of radius 1.3 μm backscatters ~70 times as much light at the 0.532-μm wavelength as a 0.7-μm droplet, suggesting that, if only submicrometer-sized droplets were present, these unusual cloud features might have gone unnoticed.
18. P. E. Ardanuy and H. L. Kyle, *J. Clim. Appl. Meteorol.* **25**, 505 (1986).
19. K. N. Liou, *Mon. Weather Rev.* **114**, 1167 (1986).

20. Support for our FIRE IFO research has come from National Science Foundation grant ATM-8914348 and National Aeronautics and Space Administration grant NAG-1-868 and for PDL development from Department of Energy grant DE-FG02ER1059 from the Atmospheric Radiation Measurement program. I thank M. T. Davies and B. S. Cho for their contributions, and various FIRE coinvestigators for making available their preliminary data.

17 March 1992; accepted 1 June 1992

State-to-State Rates for the D + $H_2(v = 1, j = 1)$ → HD(v', j') + H Reaction: Predictions and Measurements

Daniel Neuhauser,* Richard S. Judson, Donald J. Kouri,† David E. Adelman, Neil E. Shafer, Dahv A. V. Kliner,‡ Richard N. Zare†

A fully quantal wavepacket approach to reactive scattering in which the best available H_3 potential energy surface was used enabled a comparison with experimentally determined rates for the D + $H_2(v = 1, j = 1)$ → HD($v' = 0, 1, 2; j'$) + H reaction at significantly higher total energies (1.4 to 2.25 electron volts) than previously possible. The theoretical results are obtained over a sufficient range of conditions that a detailed simulation of the experiment was possible, thus making this a definitive comparison of experiment and theory. Good to excellent agreement is found for the vibrational branching ratios and for the rotational distributions within each product vibrational level. However, the calculated rotational distributions are slightly hotter than the experimentally measured ones. This small discrepancy is more marked for products for which a larger fraction of the total energy appears in translation. The most likely explanation for this behavior is that refinements are needed in the potential energy surface.

Ultimately, the test of any theory is its predictive power. In chemistry, theoretical calculations based on first principles have been applied to static properties of molecules with great success. However, theoretical calculations of dynamical properties have met with less success because of the large number of quantum mechanical (QM) scattering channels in such processes. Recent experimental advances have permitted the study of the H + H_2 reaction and its isotopic analogs at a level of detail previously not possible (*1–9*). Corresponding advances in theoretical techniques have allowed these new measurements to be compared with exact QM calculations at total energies up to 1.82 eV (*10–22*). Calculations for a range of total energies have been restricted to energies below 1.35 eV (*10, 12–14, 18*), whereas results for reactions in which the H_2 was vibrationally excited have been obtained only for total energies ranging from 0.82 to 1.35 eV (*18*) and for 1.82 eV (*16, 21*). The QM calculations (*10–14, 18, 20*) agree well with integral cross section measurements (*1–3, 8*) in the total energy regime below 1.5 eV.

Significant differences have been found between experiment (*5, 8*) and theory (*16, 21*) at the higher total energy of 1.82 eV. Two factors may influence this comparison: (i) the theoretical calculations did not fully simulate the experimental conditions; and (ii) the experimental results may have been impaired to some extent by space-charge effects caused by ion production in the use of DBr as a photolytic source of fast D atoms. Consequently, it was not possible to determine whether the differences between experiment and theory were caused by experimental error, the incomplete simulation of the experiment, the potential energy surface (PES), or the accuracy of the QM calculations. The theoretical predictions were essentially unchanged in a subsequent more accurate study (*22*); however, these calculations also did not include a full simulation of the experimental conditions. At such high energies, it may well be that the PES is less reliable for these comparisons with experiment because regions of greater anisotropy and anharmonicity can be sampled, that is, experiments at lower energies may be less sensitive to inaccuracies in the PES.

Existing noniterative time-independent quantal scattering methods rapidly become computationally intensive at higher total energies because of the increase in the number of quantum channels (*10–22*). We report here theoretical results obtained with a newly developed wavepacket approach (*21, 23–26*) to exact scattering dynamics that extends the predictive power of theory to higher energies and more complex scattering systems; consequently, a full simulation of the experimental conditions was feasible. We also report new state-to-state integral cross section measurements of the D + H_2(v

D. Neuhauser, James Franck Institute, University of Chicago, Chicago, IL 60637.
R. S. Judson, Sandia National Laboratory, Center for Computational Engineering, Livermore, CA 94551–0969.
D. J. Kouri, Department of Chemistry and Department of Physics, University of Houston, Houston, TX 77204–5641.
D. E. Adelman, N. E. Shafer, D. A. V. Kliner, R. N. Zare, Department of Chemistry, Stanford University, Stanford, CA 94305–5080.

*Present address: Department of Chemistry, University of California, Los Angeles, CA 90024.
†To whom correspondence should be addressed.
‡Present address: Department of Chemistry, University of Minnesota, Minneapolis, MN 55455.

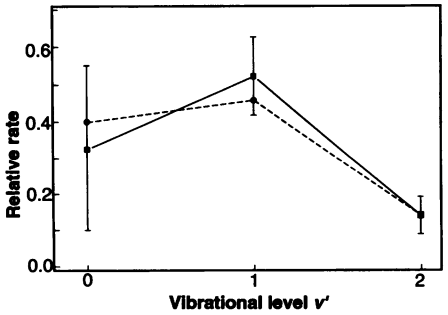

Fig. 1. Comparison of experimental and theoretical relative vibrational population distributions for the reaction D + $H_2(v = 1, j = 1) \rightarrow HD(v', j')$ + H at $E_{rel} \approx 1.4$ eV. The experimental (*9*) data (squares connected by solid lines) are recorded by using a variable-wavelength photolysis source, and the theoretical calculations (*26*) (circles connected by dashed lines) are obtained with the wavepacket approach. The experimental error bars represent one standard deviation.

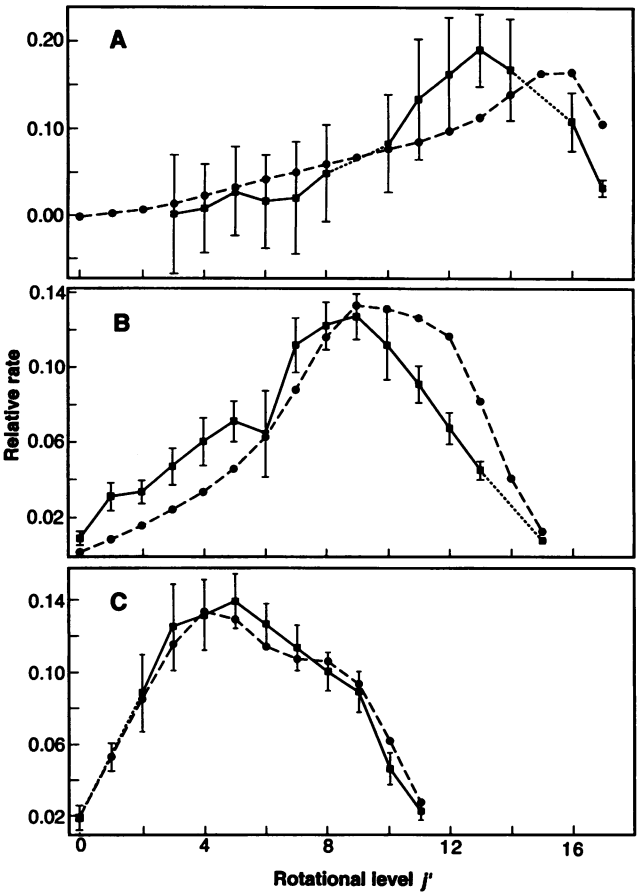

Fig. 2. Comparison of experimental and theoretical relative rotational population distributions for the reaction D + $H_2(v = 1, j = 1) \rightarrow HD(v', j')$ + H for a variable-wavelength photolysis source: (**A**) $HD(v' = 0, j')$ at $E_{rel} \approx 1.5$ eV; (**B**) $HD(v' = 1, j')$ at $E_{rel} \approx 1.4$ eV; and (**C**) $HD(v' = 2, j')$ at $E_{rel} \approx 1.3$ eV. The experimental data (*8, 9*) are represented by squares connected by solid lines; the error bars are one standard deviation. The theoretical calculations (*26*) are represented by circles connected by dashed lines. Dotted lines connect the populations of levels adjacent to a level for which the population was not measured.

$= 1, j = 1$) reaction (where v is the vibrational quantum number and j is the rotational quantum number) in which DI was used as the fast D atom photolytic precursor, thus significantly reducing the space-charge effects associated with the DBr precursor. Comparison of the new experimental results with the calculations of the wavepacket approach yields a definitive test of theory at higher total energies than previously possible.

A combination of laser techniques has enabled true state-to-state experiments for the H + H_2 reaction family to be carried out. The D + $H_2(v = 1, j = 1) \rightarrow HD(v' = 0, 1, 2; j')$ + H reaction rates have been measured, in which the H_2 reagent was prepared in the ($v = 1, j = 1$) state by stimulated Raman pumping (*7–9*), and fast D atoms were produced by laser photolysis of DBr or DI. In these experiments the DBr(DI) and H_2 were mixed with He in a reservoir and then flowed into a high-vacuum chamber through a pulsed supersonic nozzle. The same laser both generated the fast D atoms needed to initiate the reaction and ionized the nascent HD product through (2 + 1) resonance-enhanced multiphoton ionization (REMPI) (*27*), in which a two-photon transition connects the X state to the E, F state of HD that is subsequently ionized by a one-photon transition. The REMPI detection scheme has been calibrated against an effusive high-temperature nozzle (*27*) such that relative quantum-state populations can be obtained from the measured ion signals. A shuttered time-of-flight mass spectrometer was used to detect the HD^+ ions (*3, 28*). Because the same laser effected the photolysis and ionization steps, E_{rel} varied as a function of product state detected. By replacing the DBr precursor (E_{rel} = 0.95 to 1.07 eV) used in the earlier experiments with DI, higher values of E_{rel} are obtained [1.38 to 1.54 eV for $HD(v' = 0)$, 1.31 to 1.43 eV for $HD(v' = 1)$, and 1.26 to 1.32 eV for $HD(v' = 2)$]. At these relative collision energies and with 0.52 eV in the H_2 reagent vibration, the reaction accesses regions of the PES far removed from the minimum energy path. Furthermore, the use of DI significantly reduces the previously noted (*7, 8*) space-charge effects associated with the DBr precursor.

The broad range and high total energies associated with these experiments make the corresponding theoretical calculations extremely difficult. Noniterative, time-independent basis set expansion methods (*10–14, 17–20, 22*) have been the only means previously available for carrying out sophisticated fully converged, three-dimensional reactive QM scattering calculations. Although applicable to reactions at lower total energies, such methods become highly computationally intensive under the present experimental conditions. New approaches are needed to compare theory and experiment at these high energies in which a large number of reaction channels are open.

Among the theoretical techniques used, the newly developed time-dependent wavepacket approach (*21, 23, 24*) has four attractive features. First, calculations are performed only for the initial state of interest, whereas noniterative time-independent basis set methods necessarily include all initial states accessible at a given energy. Second, a single propagation of the wavepacket yields results at many energies, thereby significantly reducing the number of calculations required. Third, a grid representation is used so that the potential energy is calculated by simple multiplication. Fourth, the wavepacket can be propagated by using the Jacobi scattering coordinates of a single arrangement. Perhaps most importantly, the associated numerical complexity grows roughly linearly with the number of grid points. This is a marked advantage over the noniterative basis set methods, in which the Hamiltonian matrix must be inverted and the computational effort scales as N^3, where N is the size of the basis set used.

Recent developments in the time-dependent approach include accurate methods for evaluating the kinetic energy terms and a mixed grid and close-coupling approach for representing the wave function. When these methods are coupled with an accurate algorithm for propagating the wavepacket, the resulting approach is decisively the most efficient available for simulating inelastic molecular collisions at high energies. For reactive collisions, the major difficulty is the presence of multiple asymptotic arrangements. Large grids are then ostensibly necessary for representing the wave function before and after the scattering event. This difficulty is circumvented (*23–25*) in three ways: (i) by using projection operators to couple the one-channel wave function in the reactant arrangement to the many-chan-

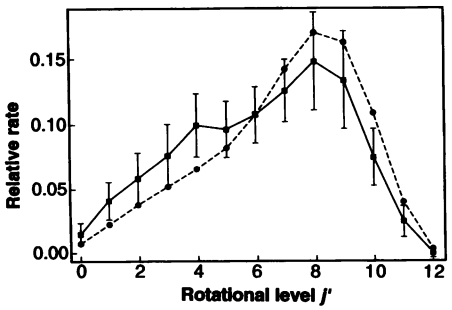

Fig. 3. Comparison of experimental and theoretical relative rotational population distributions for the reaction D + $H_2(v = 1, j = 1) \rightarrow$ HD($v' = 1, j'$) + H for a fixed-wavelength photolysis source (E_{rel} = 0.8 eV). The experimental data (*9*) are represented by squares connected by solid lines; the error bars are one standard deviation. The theoretical calculations (*26*) are represented by circles connected by dashed lines.

nel wave function in the interaction region so that a many-channel representation is needed only in a small region; (ii) by calculating accurate state-to-state probabilities with an overlap-integral expression for the scattering matrix that enables the asymptotic scattering probabilities to be calculated from the wavepacket within and just outside of the interaction region; and (iii) by introducing functions that absorb the wavepacket as it scatters from the interaction region, thereby reducing the wavepacket propagation time.

The computational efficiency of the time-dependent wavepacket approach permits a complete simulation of the D + H_2 experiments (*26*). Specifically, the theoretical calculations include: (i) the variation in the relative collision energy as a function of HD rovibrational state detected; (ii) the experimental relative collision energy spread (~0.07 eV full-width at half-maximum); and (iii) the fast and slow D atom contributions corresponding to the concurrent production of $I(^2P_{3/2})$ and $I(^2P_{1/2})$ in the photolysis of DI. In order to perform a quantitative comparison between theory and experiment, we must have a well-characterized experimental procedure. Numerous tests are carried out to check for possible sources of experimental error. Among the most important of these checks are: (i) verification of the validity of the procedure used to extract the D + $H_2(v = 1, j = 1)$ distributions (*8*); (ii) use of two photolytic D atom sources (DI and DBr) (*8, 9*); (iii) determination that HD product fly-out from the detection volume is not perturbing the rotational distributions (*9*); and (iv) use of an independent, fixed-wavelength photolysis source geometry (*9*). Consequently, we are confident that neither experimental error nor incomplete modeling of the experimental initial conditions is the source of the remaining discrepancies between theory and experiment.

Comparisons of the experimental and theoretical results for the reaction D + $H_2(v = 1, j = 1) \rightarrow$ HD(v', j') + H are represented in Figs. 1 to 3. Because relative populations are measured, the experimental and theoretical distributions in each of the comparisons are normalized to the sum of the populations of their common levels. The distributions presented in Figs. 1 and 2 are measured with a variable-wavelength photolysis source, as described above. However, the D + $H_2(v = 1, j = 1) \rightarrow$ HD($v' = 1, j'$) + H at E_{rel} = 0.8 eV rotational distribution displayed in Fig. 3 was recorded with a fixed-wavelength photolysis arrangement. For this geometry, an independent laser pulse was added to generate the fast D atoms through photolysis of DI. This procedure allows the DI photolysis and HD ionization steps to be decoupled.

Very good agreement is observed between experiment and theory for the vibrational distribution (see Fig. 1); they agree within the experimental error bars for each vibrational level. For the rotational distributions, however, the extent of agreement varies from moderately good (Fig. 2, A and B) to quantitative (Figs. 2C and 3). The very good agreement observed for the HD($v' = 2, j'$) distribution at $E_{rel} \approx 1.3$ eV (Fig. 2C) and HD($v' = 1, j'$) distribution at E_{rel} = 0.8 eV (Fig. 3) shows that the discrepancies in Fig. 2, A and B, are not caused by the vibrational state of the HD product. As the fraction of energy grows in the HD product translational degree of freedom, the theoretical distributions become increasingly hotter than the corresponding experimental ones (Figs. 2 and 3). Thus, both the overall shape and the peak of the distributions are in good agreement for the HD($v' = 2, j'$) distribution at $E_{rel} \approx 1.3$ eV and the HD($v' = 1, j'$) distributions at E_{rel} = 0.8 eV (Figs. 2C and 3). In contrast, neither the shape nor the peak of the distributions is well matched by theory for the HD($v' = 0, j'$) distribution at $E_{rel} \approx 1.5$ eV and the HD($v' = 1, j'$) distribution at $E_{rel} \approx 1.4$ eV (Fig. 2, A and B). Specifically, the calculated distributions peak one to two quanta higher than the measured ones in Fig. 2B and two to three quanta in Fig. 2A.

The consistency of the experimental and theoretical results for the vibrational distribution (Fig. 1) and for the rotational distributions HD($v' = 1, j'$) at E_{rel} = 0.8 eV (Fig. 3) and HD($v' = 2, j'$) at $E_{rel} \approx 1.3$ eV (Fig. 2C) suggests that the observed discrepancies do not arise from an error in the QM scattering calculations. Instead, we believe the differences are most likely attributable to inaccuracies in the PES used, which was the double many-body expansion (*29*). This hypothesis is consistent with the good agreement observed for the lower energy reactions, because the high energies accessed in these experiments allow the reactants to explore regions of the PES far removed from the minimum energy path of the reaction. The PES is not as well characterized in these regions because ab initio points that are used to generate the surface are concentrated around the minimum energy path. Buntin *et al.* (*4, 5*) and Continetti *et al.* (*6*) measured differential cross sections for the D + H_2 reaction and simulated the experiments with the QM calculations of Zhao *et al.* (*18*) and of Zhang and Miller (*10, 14*). These workers also found discrepancies that they attributed to errors in the H_3 PES.

As the above comparisons demonstrate, the new wavepacket approach is able to provide a full simulation of the dynamics of the D + $H_2(v = 1, j = 1) \rightarrow$ HD($v' = 0, 1, 2; j'$) + H reaction at high total energies. The accuracy of these calculations is apparently limited only by the accuracy of the PES for the reaction and the validity of the assumption that this reaction is electronically adiabatic (*30*). The wavepacket approach has matured to the stage where it affordably yields complete dynamical information. Furthermore, the reduced computational effort, relative to the noniterative time-independent basis set expansion methods, establishes the wavepack approach as a powerful method for predicting the dynamics of systems with high energy or complexity or both.

REFERENCES AND NOTES

1. D. P. Gerrity and J. J. Valentini, *J. Chem. Phys.* **81**, 1298 (1984).
2. H. B. Levene *et al.*, *Chem. Phys. Lett.* **143**, 317 (1988).
3. K.-D. Rinnen, D. A. V. Kliner, R. N. Zare, *J. Chem. Phys.* **91**, 7514 (1989).
4. S. A. Buntin, C. F. Giese, W. R. Gentry, *ibid.* **87**, 1443 (1987).
5. _____, *Chem. Phys. Lett.* **168**, 513 (1990).
6. R. E. Continetti, B. A. Balko, Y. T. Lee, *J. Chem. Phys.* **93**, 5719 (1990).
7. D. A. V. Kliner and R. N. Zare, *ibid.* **92**, 2107 (1990).
8. D. A. V. Kliner, D. E. Adelman, R. N. Zare, *ibid.* **95**, 1648 (1991).
9. D. E. Adelman, N. E. Shafer, D. A. V. Kliner, R. N. Zare, unpublished work.
10. J. Z. H. Zhang and W. H. Miller, *Chem. Phys. Lett.* **153**, 465 (1988).
11. M. Mladenovic *et al.*, *J. Phys. Chem.* **92**, 7035 (1988).
12. D. E. Manolopoulos and R. E. Wyatt, *Chem. Phys. Lett.* **159**, 123 (1989).
13. J. M. Launay and M. L. Dourneuf, *ibid.* **163**, 178 (1989).
14. J. Z. H. Zhang and W. H. Miller, *J. Chem. Phys.* **91**, 1528 (1989).
15. W. H. Miller, *Annu. Rev. Phys. Chem.* **41**, 245 (1990).
16. H. Buchenau, J. P. Toennies, J. Arnold, J. Wolfrum, *Ber. Bunsenges. Phys. Chem.* **94**, 1231 (1990).
17. N. C. Blais, M. Zhao, D. G. Truhlar, D. W. Schwenke, D. J. Kouri, *Chem. Phys. Lett.* **166**, 11 (1990).
18. M. Zhao, D. G. Truhlar, D. W. Schwenke, D. J. Kouri, *J. Phys. Chem.* **94**, 7074 (1990).
19. J. V. Michael, J. R. Fisher, J. M. Bowman, Q. Sun, *Science* **249**, 269 (1990).
20. M. D'Mello, D. E. Manolopoulos, R. E. Wyatt, *J. Chem. Phys.* **94**, 5985 (1991).
21. D. Neuhauser, *ibid.* **95**, 4927 (1991).
22. S. L. Mielke, R. S. Friedman, D. G. Truhlar, D. W.

Schwenke, *Chem. Phys. Lett.* **188**, 359 (1992).
23. D. Neuhauser, M. Baer, R. S. Judson, D. J. Kouri, *ibid.* **169**, 372 (1990).
24. D. Neuhauser, *J. Chem. Phys.* **93**, 7836 (1990).
25. _____, R. S. Judson, M. Baer, D. J. Kouri, in *Advances in Molecular Vibrations and Collision Dynamics*, J. M. Bowman, Ed. (JAI Press, Greenwich, CT, in press), vol. 2.
26. D. Neuhauser, R. S. Judson, D. J. Kouri, unpublished work.
27. K.-D. Rinnen, D. A. V. Kliner, R. N. Zare, W. M. Huo, *Isr. J. Chem.* **29**, 369 (1989); K.-D. Rinnen, M. A. Buntine, D. A. V. Kliner, R. N. Zare, W. M. Huo, *J. Chem. Phys.* **95**, 214 (1991).
28. K.-D. Rinnen, D. A. V. Kliner, R. S. Blake, R. N. Zare, *Rev. Sci. Instrum.* **60**, 717 (1989).
29. A. J. C. Varandas *et al.*, *J. Chem. Phys.* **86**, 6258 (1987).
30. B. Lepetit and A. Kuppermann, *Chem. Phys. Lett.* **166**, 581 (1990).
31. D.N. is a James Franck postdoctoral fellow, D.E.A. is an NSERC postgraduate fellow, and D.A.V.K. is an NSF postdoctoral fellow. This work was supported by several sources: R.S.J. acknowledges support from the DOE under the contract DE-AC04-76DP00789; D.J.K. from the NSF under grant NSF CHE-89-07429, and through a grant of supercomputer resources from the NSF Division of Advanced Scientific Computing at NASA-Ames; and R.N.Z. from the NSF under grant NSF CHE-89-21198.

2 April 1992; accepted 16 June 1992

Magnetoferritin: In Vitro Synthesis of a Novel Magnetic Protein

Fiona C. Meldrum, Brigid R. Heywood, Stephen Mann*

The iron storage protein ferritin consists of a spherical polypeptide shell (apoferritin) surrounding a 6-nanometer inorganic core of the hydrated iron oxide ferrihydrite ($5Fe_2O_3 \cdot 9H_2O$). Previous studies have shown that the in vitro reconstitution of apoferritin yields mineral cores essentially identical to those of the native proteins. A magnetic mineral was synthesized within the nanodimensional cavity of horse spleen ferritin by the use of controlled reconstitution conditions. Transmission electron microscopy and electron diffraction analysis indicate that the entrapped mineral particles are discrete 6-nanometer spherical single crystals of the ferrimagnetic iron oxide magnetite (Fe_3O_4). The resulting magnetic protein, "magnetoferritin," could have uses in biomedical imaging, cell labeling, and separation procedures.

The ability of ferritin to sequester and store iron in a bioavailable form arises from a quaternary structure of 24 polypeptide subunits assembled into a spherical hollow shell that is penetrated by two types of intersubunit channels (*1*). The mechanisms by which iron is accumulated within the 8-nm internal cavity have been elucidated through reconstitution experiments of recombinant apoferritins modified by site-directed mutagenesis (*2*). In brief, two key sites have been implicated: a ferroxidase center residing in the intrahelical domain of H-chain subunits (*3*) and a nucleation site comprising three Glu residues on the cavity surface. These sites appear to act cooperatively in affecting the kinetics of iron oxide deposition such that mineralization occurs specifically within the protein cavity and not in bulk solution. Such precise molecular control of inorganic precipitation within a confined volume could be generally relevant to the synthesis of inorganic clusters and nanoparticles. We have recently shown that Mn(III) oxide cores can be reconstituted in ferritin by incubation of apoferritin molecules with aqueous Mn(II) under controlled reaction conditions (*4*).

School of Chemistry, University of Bath, Bath BA2 7AY, United Kingdom.

*To whom correspondence should be addressed.

Although we have synthesized iron sulfide cores in ferritin by in situ reaction of native iron oxide cores with gaseous H_2S (*4*), the formation of iron oxide cores other than ferrihydrite has not been achieved (*5*). Indeed, it has generally been considered that the ferrihydrite structure of the biomineral is functionally important in providing a source of relatively labile iron for metabolic use. To determine the extent of structural specificity of iron oxide mineralization in ferritin, we carried out reconstitution experiments under conditions tailored to the synthesis of Fe_3O_4 (Fig. 1) (*6*). Iron was removed from native horse spleen ferritin by dialysis against thioglycolic acid at pH 4.5 (*7*). The resulting apoferritin solution was buffered at pH 8.5 and maintained at a temperature of 55° to 60°C under argon in a water bath. Ten increments of Fe(II) solution were added over 200 min (*8*). Slow oxidation was achieved during this procedure by the introduction of air into the solution with a Pasteur pipette. On completion of the Fe(II) additions, samples of the reconstituted ferritin were taken immediately for transmission electron microscopy (TEM) analysis (*9*). Several samples were left open to the atmosphere for 15 min before TEM investigation to ascertain their stability to possible oxidation in air. Some of these grids were negatively stained with 1% uranyl acetate solution to determine whether any thermal degradation of the protein had occurred and to verify that the crystals had indeed been produced within the protein shell. Protein-free control reactions, involving an analogous procedure in which 0.15 M saline was substituted for apoferritin, were also undertaken (*10*).

Addition of Fe(II) to the apoferritin solutions resulted in an initial increase in turbidity followed by a blackish discoloration after ~1 hour. The final solution remained black, and no bulk precipitation was observed. Exposure to air resulted in a red-brown coloration within a few minutes. Neither the black nor the red-brown protein solutions responded to a bar magnet placed against the side of the sample container. In contrast, a bulk white precipitate [$Fe(OH)_2$] was initially formed in the control reaction, transforming into a green gelatinous deposit and subsequently into a black and magnetic precipitate after 1 hour. The sample remained black under argon and after exposure to the atmosphere for 2 weeks.

Examination of the ferritin and control samples by TEM showed particles of remarkably different size and morphology (Fig. 2). The majority of particles synthesized in the presence of apoferritin were discrete, spherical nanometer-sized crystals (Fig. 2A) of uniform size (mean diameter = 6 nm, σ = 1.2 nm). Negative staining showed that the individual particles were surrounded by a protein shell (Fig. 2B), indicating that the discrete crystals were formed specifically within the apoferritin cavity. In contrast, particles formed in the control preparations were aggregated and heterogeneous in size (range = 4 to 70 nm) and morphology (irregular spheroidal, cubic, and cubo-octahedral) (Fig. 2C). Electron diffraction patterns identified the crys-

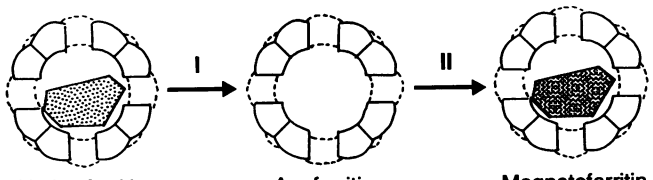

Fig. 1. Schematic showing the synthetic route to magnetoferritin. Step I involves the removal of native ferrihydrite cores from horse spleen by dialysis against thioglycolic acid, under N_2, at pH 4.5. Step II involves the reconstitution of apoferritin with Fe(II) solution under slow oxidative conditions at 60°C and pH 8.5.